Convergence and divergence in spherical harmonic series of the gravitational field generated by high-resolution planetary topography – a case study for the Moon

7 Christian Hirt[1] and Michael Kuhn[2]

8 [1]Institute for Astronomical and Physical Geodesy & Institute for Advanced Study,
9 Technische Universität München, Arcisstr 21, 80333 München, Germany

10 [2]Western Australian Geodesy Group & Department of Spatial Sciences
11 Curtin University Perth, GPO Box U1987, Perth, 6845, Western Australia

Key points
- New systematic experiments reveal behaviour of spherical harmonic series near the Moon's topography as function of resolution and altitude
- Gravity from degree-180 models free of divergence, degree-360 models partially divergent and degree-2160 models severely divergent
- New hypothesis: Local minimum in potential degree variances foreshadows series divergence inside the Brillouin-sphere

Abstract
Theoretically, spherical harmonic (SH) series expansions of the external gravitational potential are guaranteed to converge outside the Brillouin-sphere enclosing all field-generating masses. Inside that sphere, the series may be convergent or may be divergent. The series convergence behaviour is a highly unstable quantity that is little studied for high-resolution mass distributions.

Here we shed light on the behaviour of SH series expansions of the gravitational potential of the Moon. We present a set of systematic numerical experiments where the gravity field generated by the topographic masses is forward-modelled in spherical harmonics and with numerical integration techniques at various heights and different levels of resolution, increasing from harmonic degree 90 to 2160 (~61 to 2.5 km scales). The numerical integration is free from any divergence issues and, therefore, suitable to reliably assess convergence vs. divergence of the SH series.

Our experiments provide unprecedented detailed insights into the divergence issue. We show that the SH gravity field of degree-180 topography is convergent anywhere in free space. When the resolution of the topographic mass model is increased to degree 360, divergence starts to affect very high degree gravity signals over regions deep inside the Brillouin-sphere. For degree-2160 topography/gravity models, severe divergence (with several 1000 mGal amplitudes) prohibits accurate gravity modelling over most of the topography.

As a key result, we formulate a new hypothesis to predict divergence: If the potential degree variances show a minimum, then the SH series expansions diverge somewhere inside the Brillouin-sphere, and modelling of the internal potential becomes relevant.

47   **Introduction**

48   In planetary sciences, spherical harmonic (SH) series expansions are commonly used to model the
49   exterior gravitational potential of Moon, Earth, and other terrestrial planets [e.g., *Blakeley*, 1996;
50   *Balmino et al.,* 2012; *Konopliv et al.,* 2014; *Lemoine et al.,* 2014; *Wieczorek,* 2015]. The coefficients of
51   the SH series expansions can be either determined from field observations (e.g., measured gravity
52   accelerations or satellite orbit perturbations), cf. *Pavlis* [2014], or with forward modelling techniques
53   [e.g., *Rexer et al.,* 2016]. In the latter case, a model of the planetary mass distribution (e.g., surface
54   topography model together with mass-density assumptions) is used to derive the coefficients of the
55   implied gravitational field [e.g., *Rummel et al.* 1988; *Hirt and Kuhn,* 2014].

56   In either case, the SH series of the gravitational potential or functionals thereof (e.g., radial or
57   horizontal derivatives) converge outside a sphere encompassing all field-generating mass, centered
58   to the origin of the spherical coordinate system [*Hu and Jekeli*, 2015]. In the literature, this sphere is
59   known as Brillouin sphere [e.g., *Moritz*, 1980]. Inside the Brillouin sphere, however, the convergence
60   of the SH series is not guaranteed. They may converge or diverge, i.e., produce invalid numerical
61   values of gravity field functionals [e.g., *Jekeli*, 1983]. Near or at the surface of the masses, series
62   convergence must be considered an unstable property [*Krarup,* 1969], whereby "*an arbitrarily small*
63   *change*" of the mass-distribution may "*change convergence to divergence*" [*Moritz*, 1978, p19].
64   Generally, divergence is thought to occur more likely, the higher the spectral resolution of the
65   gravitational model, the more irregular the planetary body and the deeper the evaluation points are
66   located inside the Brillouin sphere [*Wang,* 1997; *Lowes and Winch,* 2012; *Hu and Jekeli,* 2015].

67   In recent time, the divergence behaviour of low-degree harmonic series expansions of gravity field
68   functionals has been intensively studied for irregularly-shaped bodies such as the Martian moons
69   Deimos and Phobos [*Hu and Jekeli,* 2015], asteroids, e.g., 433 Eros [*Hu*, 2012], Castalia and Bennu
70   [*Takahashi et al.,* 2013; *Takahashi and Scheeres,* 2014] and comets, e.g., 67P/Churyumov-
71   Gerasimenko [*Reimond and Baur,* 2016]. All studies demonstrated substantial divergence for
72   evaluation points inside the Brillouin sphere, occurring already at low spectral resolution, showing
73   the SH series unable to model the near-surface exterior gravity field of irregularly-shaped bodies with
74   adequate precision and detail.

75   Interestingly, the convergence/divergence issue associated with the synthesis of SH gravitational
76   fields of terrestrial planets in general and the Moon in particular has not received much attention
77   recently. Compared to asteroids and other such objects, the Moon and the terrestrial planets are
78   much more regular in shape, and reasonably well approximated through rotationally-symmetric
79   bodies such as a sphere (e.g., Moon) or ellipsoid (e.g., Earth). As a consequence of the more regular
80   shape compared to asteroids and other oddly shaped bodies, the free space inside the Brillouin
81   sphere is reduced [*Hu and Jekeli,* 2015]. As a result, the SH gravity models of Moon and planets tend
82   to be less prone to divergence, at least at lower resolution (also see *Werner and Scheeres* [1997],
83   p314, "*in planetary applications, the divergence may not exist or may be ignored as the body will be*
84   *nearly spherical*"). However, the situation is completely different with high-resolution gravity models,
85   as we show in this study for the Moon.

86   While the gravitational field of the Moon is now routinely modelled with higher-degree SH series
87   expansions – particularly as a result of the GRAIL gravity field mission [*Zuber et al.,* 2013; *Lemoine et*
88   *al.*, 2014; *Konopliv et al.,* 2014] – surprisingly little is known about if and where inside the Brillouin
89   sphere these series actually converge or diverge. In some cases, series convergence is taken for

90 granted even when the evaluation points are located inside the Brillouin sphere of the Moon
91 [*Goossens et al.,* 2011; *Hirt and Featherstone*, 2012; *Featherstone et al.,* 2013; *Konopliv et al.,* 2014].
92 However, divergence in the SH series of gravity field functionals may be a critical factor in high-
93 resolution planetary gravity modelling, as demonstrated in this contribution.

94 The goal of the present paper is to shed new light on the convergence vs. divergence behaviour of SH
95 series inside the Brillouin sphere, exemplified here for the external gravitational field of the Moon.
96 We present and analyse a set of systematically designed and conducted numerical experiments
97 where the gravity field of the topographic masses is forward-modelled in SH, and with numerical
98 integration (NI) techniques at different levels of resolution, increasing from degree 90 to 2160. The
99 NI is free from any divergence issues and, therefore, suitable to reliably assess the convergence vs.
100 divergence behaviour of the SH models, that are evaluated here at different altitudes (height levels)
101 inside and outside the Brillouin sphere. High-performance computing is deployed to reduce
102 discretisation errors in the NI on the one hand. Spectral forward modelling with multiple band-widths
103 ensures rigorous spectral consistency between the NI and the SH forward gravity model on the other
104 hand.

105 Because of their widespread application in planetary sciences, the present study focuses on exterior
106 spherical harmonic series, in our case, of gravity values. We acknowledge that some studies discuss
107 spheroidal (ellipsoidal) instead of spherical harmonics to improve the convergence region of the
108 gravity field series expansions [*Hu and Jekeli*, 2015; *Reimond and Baur,* 2016]. The ellipsoidal
109 approach, however, does not appear promising for the Moon, given its negligible flattening.

110 Internal (interior) spherical harmonic series might be an alternative that avoid divergence associated
111 with the widely used exterior series. In local applications, interior harmonics are sometimes used
112 because they guarantee convergence in a sphere exterior and tangent to the planetary surface
113 [*Takahashi and Scheeres*, 2014, p171]. However, also a combination of interior with exterior
114 harmonics (that is, the 2-potential method) can be a suitable means to obtain gravity values free of
115 divergence, not only locally, but globally. In this approach, widely used for electrostatic field
116 modelling [*Jackson*, 1962], but not yet so much for gravitational potential fields, there are two series
117 expansions evaluated when the computation point resides inside the Brillouin-sphere. The mass
118 below the computation point generates the external potential, and the mass above the computation
119 point produces the internal potential [also see *Takahashi et al.* 2013, Fig. 4 ibid]. The correct gravity
120 value is obtained as sum of both potentials, and convergence issues disappear (*Bruce Bills*, pers.
121 comm. 2017), see also discussion in Sect. 4.

122 A number of studies discuss or encounter the topic of series convergence vs. divergence in the
123 context of Earth's gravity field [e.g., *Moritz,* 1961; 1978; 1980; *Sjöberg*, 1980; *Jekeli,* 1983; *Wang,*
124 1997; *Shen*, 2009; *Hirt et al.*, 2016]. However, most of these focus on gravity modelling with lower
125 resolution than considered here. Also given the markedly different surface topographies and shape
126 of Earth and Moon, previous results for Earth are not necessarily indicative for the Moon, and this
127 statement is corroborated in the present paper.

128 **2. Data and methods**

129 **2.1 Topographic mass models**

130 Topographic mass models are the input data for the gravity forward modelling. They have two
131 components, one is the geometry and the other the density of the mass-distribution. In our work,
132 they are constructed based on high-resolution shape maps from the Lunar Orbiter Laser Altimeter
133 (LOLA) instrument [*Smith et al.,* 2010] along with a mass-density value derived from GRAIL gravity
134 mission results [*Zuber et al.*, 2013]. We use the degree-2600 MoonTopo2600pa.shape model of the

135   Moon (Wieczorek [2015], file available via http://markwieczorek.github.io/web) that is a SH
136   expansion of the LOLA 1/64° global grid (file LDEM_64_PA.IMG of March 15, 2013 from the Planetary
137   Data System, http://pds-geosciences.wustl.edu). The shape model is given in the principal axis (PA)
138   coordinate system that is consistent with that of GRAIL gravity field models (also see explanations
139   given in the meta-data file LDEM_64_PA.LBL). Planetary radii R_T are computed from shape model's
140   fully-normalized SHCs $(\bar{C}_{nm}, \bar{S}_{nm})$ via

$$R_T = \sum_{n=0}^{N_{max}^T} \sum_{m=0}^{n} (\bar{C}_{nm} \cos m\lambda + \bar{S}_{nm} \sin m\lambda) \bar{P}_{nm} (\sin \varphi) \tag{1}$$

141

142   where $\bar{P}_{nm}$ are the fully-normalized Associated Legendre Functions (ALFs) of harmonic degree n and
143   order m, (φ, λ) denote the selenocentric latitude and longitude in the PA system and N_{max}^T is the
144   maximum degree in the series expansion. The differences $H = R_T - R$ describe the surface
145   topography of the Moon relative to a reference mass-sphere of mean radius R. In all computations,
146   a value of $R = 1,738,000$ m is used, in agreement with the reference radius of the GRAIL gravity field
147   by *Lemoine et al.* [2014] and *Konopliv et al.* [2014].

148   Our study uses six mass models, with the spectral resolution N_{max}^T of topographic masses increasing
149   from degree and order 90 (~61 km spatial scales) to 2160 (~2.5 km spatial scales), cf. Table 1. The
150   resolution of the topographic mass models are even multiples of the lowest resolution ($N_{max}^T = 90$);
151   subsequent resolution levels mostly differ by a factor of 2 (cf. Table 1). The band-widths of the mass
152   models were chosen such that divergence issues or numerical problems can be narrowed down as a
153   function of resolution, ranging from ~61 to ~2.5 km.

154   The surface topography is assigned a uniform mass density value ρ_T of 2500 kg m^{-3}. A mean density
155   value of 2550 kg m^{-3} for the lunar crust was determined by *Wieczorek et al.* [2013] through inversion
156   of GRAIL gravity data. A value of 2450 kg m^{-3} was used by *Konopliv et al.* [2014] in the computation of
157   the topographic reduction of the GRAIL data, while *Lemoine et al.* [2014] assumed a density of 2500
158   kg m^{-3} in their calculation of Bouguer gravity anomalies. As such, our adopted mass-density value ρ_T
159   is the average value used in three recent studies relying on the GRAIL mission and should be a good
160   density approximation for the lunar topography. We note that a constant mass-density value will not
161   affect the behaviour of the SH series expansions, given the density acts as a "scale factor" (Eq. 2).

162   **2.2 Gravity forward modelling**

163   **2.2.1 General remarks**

164   In our study, we apply two independent techniques to compute gravitational effects (short: gravity)
165   from topographic mass models (short: topography).

166   • The first technique is forward modelling in the spectral domain whereby the gravitational
167   potential generated by the topography is expanded into spherical harmonic (SH) series of
168   integer powers of the topography [e.g., *Chao and Rubincam*, 1989; *Wieczorek and Phillips*,
169   1998; *Hirt and Kuhn*, 2012], see Sect. 2.2.3.
170   • The second is numerical integration (NI) in the spatial domain, also known as Newtonian
171   integration [e.g., *Werner and Scheeres*, 1997; *Kuhn et al.,* 2009; *Hirt and Kuhn*, 2014], see
172   Sect. 2.2.4.

173   We apply both techniques with the strategies detailed in *Hirt and Kuhn* [2014] to reach μGal-level
174   consistency for the gravity values when divergence is absent. Both forward modelling techniques use
175   the same topographic mass model in a rigorous, mutually consistent manner. This allows us to study

176 the convergence vs. divergence behaviour in the evaluation of the SH series expansion of gravity
177 values [cf. Eq. (4)], in a straightforward way from cross-comparisons of forward-modelled gravity
178 from both techniques.   While the topography mass models are strictly band-limited to the N_{max}^T
179 values reported in Table 1, the topography-implied gravity contains signals at harmonic degrees
180 much larger than N_{max}^T [*Hirt and Kuhn,* 2014]. To ensure spectral consistency among gravity values
181 from both techniques, the additional spectral energy must be explicitly modelled in the SH approach
182 (Sect. 2.2.3), while it is implicitly accounted for in the NI (Sect. 2.2.4).

183 **Table 1.** Characteristics of the six experiments: Resolution of the topography model, oversampling in
184 the Newton integration and maximum degrees N_{max}^G and maximum powers p_{max} modelled in the
185 spectral domain

Topography model			Newton integration	Spectral gravity modelling		
N_{max}^T	Spatial Resolution (km)	Spectral Resolution (min)	Oversampling factor of topography signal	N_{max}^G modelled	N_{max}^G required ($\sigma_n^2 > 10^{-25}$)	p_{max} Modelled (needed)
90	60.6	120	240	900	400	15(7)
180	30.3	60	120	1800	900	25 (12)
360	15.2	30	60	3600	3,600	50 (40)
720	7.6	15	30	3600	>3,600	70 (50)
1080	5.1	10	20	3600	>3,600	70 (50)
2160	2.5	5	10	3600	>3,600	70 (50)

186

2.2.2 Spatial arrangement of evaluation points

188 In all cases, gravity is computed in terms of regularly-spaced latitude φ / longitude λ grid nodes with
189 5 arc-min resolution (2160 x 4320 nodes). Regarding the radii r (vertical location) of the computation
190 points, we use four different cases for each of the six N_{max}^T topography mass model, as follows:

191 • Case 1: Surface of the topography (Hsur). Evaluation points strictly reside at the surface of the
192   topography $r = R_T$. About ~50% of points have a radius smaller than R, so are located inside
193   the reference sphere.
194

195 • Case 2: Positive topographic heights (Hpos). Evaluation points reside at the surface of the
196   topography only when outside R, otherwise evaluation takes place at R. About ~50 % of points
197   are therefore airborne, e.g., above deep depressions such as the Apollo basin, or over most of
198   the lunar maria.
199

200 • Case 3: Brillouin-sphere (H11km). We use a constant altitude of 11 km above $R = 1,738$ km as
201   safe-side approximation for the different Brillouin spheres radii R_B associated with the various
202   N_{max}^T resolution levels, and thus evaluate at $r = R_B = 1,749$ km $= R + 11$km. The chosen
203   sphere safely encompasses all mass of the Moon. This also holds at high resolution,
204   considering the highest peaks are ~ 10.8 km above R).

205

206 • Case 4: GRAIL-sphere (H23km). As additional evaluation level, the average altitude of the
207   GRAIL satellites during the extended mission phase of 23 km above $R = 1,738$ km is used, so
208   $r = R_G = R + 23$ km. This places the evaluation points farther outside the field-generating
209   masses than in case 3, giving some insights into strengths of the forward-modelled signals at
210   GRAIL radius $R_G = 1,761$ km.

211 The four cases encompass scenarios where convergence may not be guaranteed for increasing
212 spectral resolution (inside Brillouin-sphere, cases 1 and 2), and those where convergence can be
213 expected (outside Brillouin-sphere, cases 3 and 4), e.g., *Hu and Jekeli* [2015].

2.2.3 Gravity from spherical harmonic series

215 In the external SH approach, the topographic potential V is computed as series expansion of integer
216 powers p of the topography [e.g., *Chao and Rubincam*, 1989; *Wieczorek*, 2015]

$$V_{nm}^{(p)} = \frac{4\pi R^3 \rho}{(2n+1)M} \frac{\prod_{i=1}^{p}(n-i+4)}{p!\,(n+3)} H_{nm}^{(p)} \tag{2}$$

$$V_{nm} = \sum_{p=1}^{p_{max}} V_{nm}^{(p)} \tag{3}$$

217 where ρ is the adopted mass-density value for the topography, M is the total mass of the Moon, R is
218 the radius of the reference sphere, p_{max} is the maximum power considered in the series, $H_{nm}^{(p)} =$
219 $(\overline{HC}_{nm}^{(p)}, \overline{HS}_{nm}^{(p)})$ denotes the SHCs of the function $(H/R)^p$ where $H = R_T - R$ are the topographic
220 heights, $V_{nm} = (\bar{C}_{nm}, \bar{S}_{nm})$ are the potential SHCs evaluated to p_{max}, and $V_{nm}^{(p)} = (\bar{C}_{nm}^{(p)}, \bar{S}_{nm}^{(p)})$ are
221 the potential SHCs implied by the individual integer powers p ($1 \leq p \leq p_{max}$) of the function
222 $(H/R)^p$. The $V_{nm}^{(p)}$ can be thought of as contribution of the p-th power of the topography to the total
223 potential V_{nm}. The convergence of the SH series with parameter p is elaborated in detail in Sect. 3.1
224 for the topographic potential models of various resolution levels.

225 The $(H/R)^p$ functions, computed in terms of Gauss-Legendre (GL) grids, are harmonically analysed
226 with the GL quadrature (GLQ), e.g., *Sneeuw* [1994]. Raising the function H/R, that is band-limited
227 from degree 0 to N_{max}^T, to integer power p gives rise to additional short-scale signals with spectral
228 energy in band of degree $N_{max}^T + 1$ to pN_{max}^T [*Hirt and Kuhn*, 2014].

229 For each power p, the grid resolution dx (constant in longitudinal direction, but variable in latitude
230 direction, cf. *Sneeuw* [1994]) is chosen such that full recovery of these additional harmonics is
231 possible: $dx = 180°/(pN_{max}^T)$. For instance, $dx = 2°$ (91 x 181 nodes) is used for $N_{max}^T = 90$, $p = 1$,
232 while $dx = 30'$ for $N_{max}^T = 90$ and $p = 4$. This is not only required to generate a largely complete
233 SH model of the topographic potential (cf. Hirt and Kuhn 2014), but also to avoid aliases that would
234 come into play if the grid resolution dx was chosen smaller than $180°/(pN_{max}^T)$.

235 The maximum grid resolution used in the SHA is 1', corresponding to degree 10,800. The GLQ
236 algorithm used is based on the SHTools package [*Wieczorek*, 2015] and software extensions as
237 described in *Rexer and Hirt* [2015]. Their extension of the GLQ algorithm utilizes the Fukushima
238 (2012) routines for stable computation of ALFs to ultra-high-degree, along with parallel processing
239 capability.

240 Gravity values δg (defined here as radial derivatives of the potential V) are computed via

$$\delta g = \frac{GM}{r^2} \sum_{n=0}^{N^G} (n+1) \left(\frac{R}{r}\right)^n \sum_{m=0}^{n} (\bar{C}_{nm} \cos m\lambda + \bar{S}_{nm} \sin m\lambda)\bar{P}_{nm}(\sin \varphi) \tag{4}$$

241

242 where GM is the product of universal gravitational constant $G \approx 6.67384 \times 10^{-11}$ m³ kg⁻¹ s⁻² and $M \approx$
243 7.346304×10^{22} kg, r is the radius of evaluation (as defined in Sect. 2.2.2), and N^G is the maximum
244 harmonic degree in the synthesis of gravity values, and N_{max}^G is the maximum degree of the V_{nm}
245 potential coefficients ($N^G \leq N_{max}^G$).

246 When the radius of evaluation is constant (cases 3 and 4), software based on the GrafLab package
247 [*Bucha and Janák*, 2013] was used, while for the cases with varying radii r across the lunar surface
248 (cases 1 and 2) a modification of the isGrafLab software [*Bucha and Janák*, 2014] was used that
249 deploys a Taylor series approach [*Hirt*, 2012] for the efficient computation of δg at the irregular
250 lunar topographic surface. Both the GrafLab and isGrafLab software utilize the *Fukushima* [2012]
251 routines for stable syntheses to ultra-high degree (e.g., 10,800).

2.2.4 Gravity from numerical integration

253 The NI technique evaluates Newton's integral [e.g., *Blakely*, 1996; *Tenzer*, 2005] in the spatial
254 domain. In this approach, the complexly-shaped topography is discretized through an ensemble of
255 regularly-shaped mass elements (e.g., prisms and tesseroids, cf. *Heck and Seitz* [2007], or polyhedra,
256 cf. *Tsoulis* [2012]), and analytical expressions are used to accurately forward-model the gravity field
257 of the mass elements. The gravitational effect of the complete topographic mass model is obtained
258 through addition (superposition) of the gravity effects implied by all mass elements.

259 To describe the geometry of the input topographic mass model, topographic radii [Eq. (1)] are
260 synthesized in terms of regularly-spaced latitude-longitude grids with a very high spatial resolution of
261 30" (21,600 x 43,200 nodes). With the chosen resolution, the topography signal is massively
262 oversampled, e.g., by a factor of 240 ($N_{max}^T = 90$) and still a reasonable oversampling of factor 10 is
263 achieved for $N_{max}^T = 2160$. The oversampling improves the spatial-domain representation of the
264 topography signal (e.g., at least 240 nodes to represent a half wave-cycle when $N_{max}^T = 90$), much
265 reducing the impact of discretisation errors on the computed gravity values. Different to the spectral
266 technique (section 2.2.3), there is no need to explicitly model short-scale gravity signals (beyond the
267 resolution of the input topography model N_{max}^T) because these are "inherently" delivered by the NI
268 approach.

269 For practical evaluation we use the highest grid resolution in the vicinity of each computation point
270 and lower the grid resolution for remote masses. At each field (=computation) point, the numerical
271 integration uses 30-arc-sec resolution within a 2 degree radius, 1-arc-min resolution within 5 degree
272 radius, 3-arc-min resolution within a 15 degree radius and a 15-arc-min grid resolution for all grid
273 points within 15 to 180 degree spherical distance to the computation point. This results in the
274 evaluation of about 1.25 M mass elements for each computation point, and ensures that the lunar
275 topographic masses are completely considered in our (full-scale) numerical integration. The use of
276 lower resolutions at some distance from the computation point is permissible considering the
277 quadratic attenuation of gravity with distance (e.g. Forsberg 1984). Importantly, the selected
278 resolutions result in approximation errors that are at most at the microGal level when applied to the
279 extreme case of a spherical shell with a thickness of 10 km.
280
281 We deployed Curtin University's in-house Newton integrator (as described in, e.g., *Kuhn and Hirt*
282 [2016]) that uses a combination of prisms (near the computation point) and tesseroids (for distant
283 masses), along with the concept of residual spherical shell integration [*Kuhn et al.*, 2009] to limit the
284 vertical extension of mass elements near the computation points. For the NI, advanced
285 computational resources (made available by Western Australia's iVEC supercomputing facility) were
286 utilized and a total of ~150,000 CPU hours used. Gravity values were computed at 5' resolution from
287 each of the six topographic mass distributions (Table 1) at the four different levels of evaluation
288 heights defined in Sect. 2.2.2. Importantly, the numerical values of the constants (G, R, ρ) used in
289 the NI are the same as in the SH modelling, ensuring consistency among both methods.

3. Numerical study

3.1 Spectral analyses

292   This section provides insight into the spectral constituents and characteristics of the six SH
293   topographic potential models (Table 1). To investigate the spectral characteristics, we use
294   dimensionless potential degree variances (e.g. Rapp 1989)

$$\sigma_n^2 = \sum_{m=0}^{n} (\bar{C}_{nm}^2 + \bar{S}_{nm}^2) \tag{5}$$

295   which are a measure of the spectral energy of the forward-modelled potential at a given harmonic
296   degree n. Accordingly, degree variances are computed for the individual potential contributions
297    $C_{nm}^{(p)}, \bar{S}_{nm}^{(p)}$ with Eq. 5. Given there is no dependency on the radii of the field points, all potential
298   coefficients from Eq. 2 and 3 and their power spectra from Eq. 5 refer to the reference sphere with
299   the adopted reference radius R = 1738,000 m.
300

301   For each of the six models, Fig. 1 displays the degree variances σ_n^2 for the individual contributions
302    $V_{nm}^{(p)}$ of the integer power p (various colors) to the (total) topographic potential V_{nm} (black lines). For
303   instance, Fig. 1a shows that potential implied by the $N_{max}^T = 90$ topography was computed through
304   summation of the contributions made by the first 15 integer powers (Eq. 3) up to a maximum degree
305    $N_{max}^G = 900$. According to the contribution scheme described in *Hirt and Kuhn* [2014], power $p = 1$
306   contributes to $N_{max}^T = 90$, power $p = 2$ up to $2N_{max}^T = 180$, and $p = 15$ to degree 1350. Any
307   spectral power at degrees > N_{max}^T originates from raising the topography to integer powers $p \geq 2$,
308   and it is these "extra" short-scale energies that must be explicitly modelled in the SH approach if
309   consistency with NI-based forward modelling is sought.

310   For a comparatively low N_{max}^T value of 90, Fig. 1a supports the postulation made in *Wieczorek* [2015]
311   that the contribution made by "*each succeeding term is smaller than the previous*". Fig. 1a reveals for
312   the degree-90 model fast convergence of the series expansion (Eq. 3) with increasing p. For instance,
313   the potential contribution of $p = 5$ does not exceed a degree variance $\sigma_n^2 = 10^{-20}$, and for $p > 10$
314   the spectral power is negligibly small ($\sigma_n^2 < 10^{-30}$), compared to the gravity signal associated with
315   the linear term ($p = 1$) that contributes the bulk of spectral energy ($\sigma_n^2 > 10^{-15}$) to V_{nm}. Assuming
316   that potential contributions with an associated signal strength $\sigma_n^2 < 10^{-25}$ are rather insignificant for
317   the forward modelling (e.g., Hirt and Kuhn 2012), Fig. 1a shows that series convergence is reached
318   for $p_{max} \approx 7$ and $N_{max}^G \approx 400$, with a monotonic decline of σ_n^2 with harmonic degree n visible over
319   the whole spectrum.

320   When the spectral resolution N_{max}^T of the input topography model is increased, the convergence
321   behaviour of the SH series (Eqs. 2, 3) changes considerably. For instance the computation of the
322   implied potential from a $N_{max}^T = 180$ model requires $p_{max} \approx 12$ and $N_{max}^G \approx 900$ to converge (Fig.
323   1b). Further doubling to $N_{max}^T = 360$ (Fig. 1c) results in a much slowed-down convergence, with
324   several integer powers to $p_{max} \approx 40$ required to converge over the band-width considered (here
325    $N_{max}^G = 3600$, corresponding to the first ten multiples of the input band-width N_{max}^T). The spectral
326   energy of the potential generated by $N_{max}^T = 360$ is seen to steadily, but very slowly decline beyond
327   degree 360, with an energy level of $\sigma_n^2 = 10^{-20}$ reached near $n \approx 1300$, and $\sigma_n^2 = 10^{-22}$ near $n \approx$
328   3,600 (black curve in Fig. 1c).

329   From $N_{max}^T = 360$ (Fig. 1c) to $N_{max}^T = 720$ (Fig. 1d), the spectral characteristics of the potential
330   models change substantially. Instead of monotonically decreasing energy, the potential generated by
331   the $N_{max}^T = 720$ topography shows a decrease to $n \approx 1300$, followed by a monotonic *increase* in
332   spectral energy for degrees $n > \sim1300$ (cf. Fig. 1d). For the potential spectra of the $N_{max}^T =$
333   1080 (2160) topography models, the increase in spectral energy enters at lower degree ($n \approx 800$)
334   and is even more pronounced (Figs. 1e, 1f). Given that gravity signal strengths are generally expected
335   to decay with resolution [e.g., *Rapp,* 1989], this behaviour is surprising. It may foreshadow

336 divergence associated with the short-scale constituents of potential model in the spatial domain
337 inside the Brillouin-sphere (Sect. 3.2). As another explanation for this observation, the spectral-
338 domain technique [Eqs. (2), (3)] extremely amplifies the short-scale potential constituents (at the
339 chosen reference sphere with R the spectra in Fig. 1 refer to), such that they attenuate "correctly"
340 when gravity signals are computed outside the Brillouin sphere. Evidence supporting both
341 hypotheses are obtained from our spatial-domain analyses in Sect 3.2.

342 A detailed look at the spectral energy associated with the various integer powers of the topography
343 shows that

- 344 for $N_{max}^T \geq 360$, the largest potential contribution at short scales (e.g., $n \approx 3{,}600$) is being
  345 made by higher-order powers, e.g., $p \approx 35$ when $N_{max}^T = 360$, and $p \approx 25$ when $N_{max}^T =$
  346 2160 (cf. Figs. 1c and 1f), and

- 347 the degree variances of V_{nm} may exceed those of any of the single contributions $V_{nm}^{(p)}$ by two
  348 orders of magnitude at high harmonic degrees (e.g., $n \approx 2{,}000$), which is a result of the
  349 summation of several individual p −contributions of similar spectral power (compare black
  350 vs. colour lines in Figs. 1c to 1f).

351 Figure 1 also suggests that at any given degree n, the V_{nm} coefficients are spectrally completely
352 modelled when the degree variance associated with the p_{max}-th contribution is at least 7-8 orders of
353 magnitude below the maximum contribution. Using this criterion for the convergence of the
354 summation over powers p (Eq. 2), the V_{nm} coefficients are completely modelled for any
355 $0 \leq n \leq 3600$, when $p_{max} \geq 50$. Note that coefficients beyond $n > 3600$ are not further taken into
356 account in our work because (i) they would possibly require very large integer powers p which might
357 be swamped by under/overflow errors in a double-precision computation environment (M. Rexer,
358 pers. comm. 2016), and (ii) they don't seem to influence the series behaviour in a general sense.

359 As a side note, Fig. 1 suggests that postulations made in Wieczorek [2015] that "each succeeding
360 term is smaller than the previous" and similarly in Wieczorek and Phillips [1998] that "the magnitude
361 of each successive term […] is smaller than the previous one" hold only up to some certain harmonic
362 degree. When the potential models reach or exceed a certain level of detail, the energy of several
363 succeeding terms is larger than of the previous at high degrees as is seen from the spectral
364 composition of the higher-degree models (Figs. 1c to 1f). As a result, there is an (apparent) increase
365 in short-scale energy visible in the power spectra. We emphasize that all power spectra shown in Fig.
366 1 refer to the reference sphere, so are not representative for the spectrum of, e.g., gravity values
367 evaluated outside the Brillouin-sphere, that would be declining with increasing harmonic degree. We
368 note that in the context of ultra-high resolution Earth gravity modelling, the study by Balmino et al.
369 [2012] made similar observations regarding the contributions of the higher-order powers to Earth's
370 topographic potential.

371 Fig. 2 finally shows the spectra of the six topographic potential models, as computed with Eq. (3)
372 together with the degree variances of the GRAIL gravity model GRGM900C [*Lemoine et al.,* 2014].
373 Given (i) our forward-modelling constants R, G, M (Section 2.3) were adopted based on the constants
374 of the GRGM900C model, (ii) the average mass-density of the Moon's crust well approximated by our
375 adopted density value (cf. Section 2.2) and (iii) the majority of the GRAIL-measured gravity signals is
376 well explained through gravity from topography [e.g., *Zuber et al.,* 2013], the spectra of the forward
377 models and GRAIL model are – as would be expected – in reasonably close agreement (Fig. 2). See
378 e.g., Lemoine et al. [2014] for a more detailed analysis of differences between observed and
379 modelled gravity.
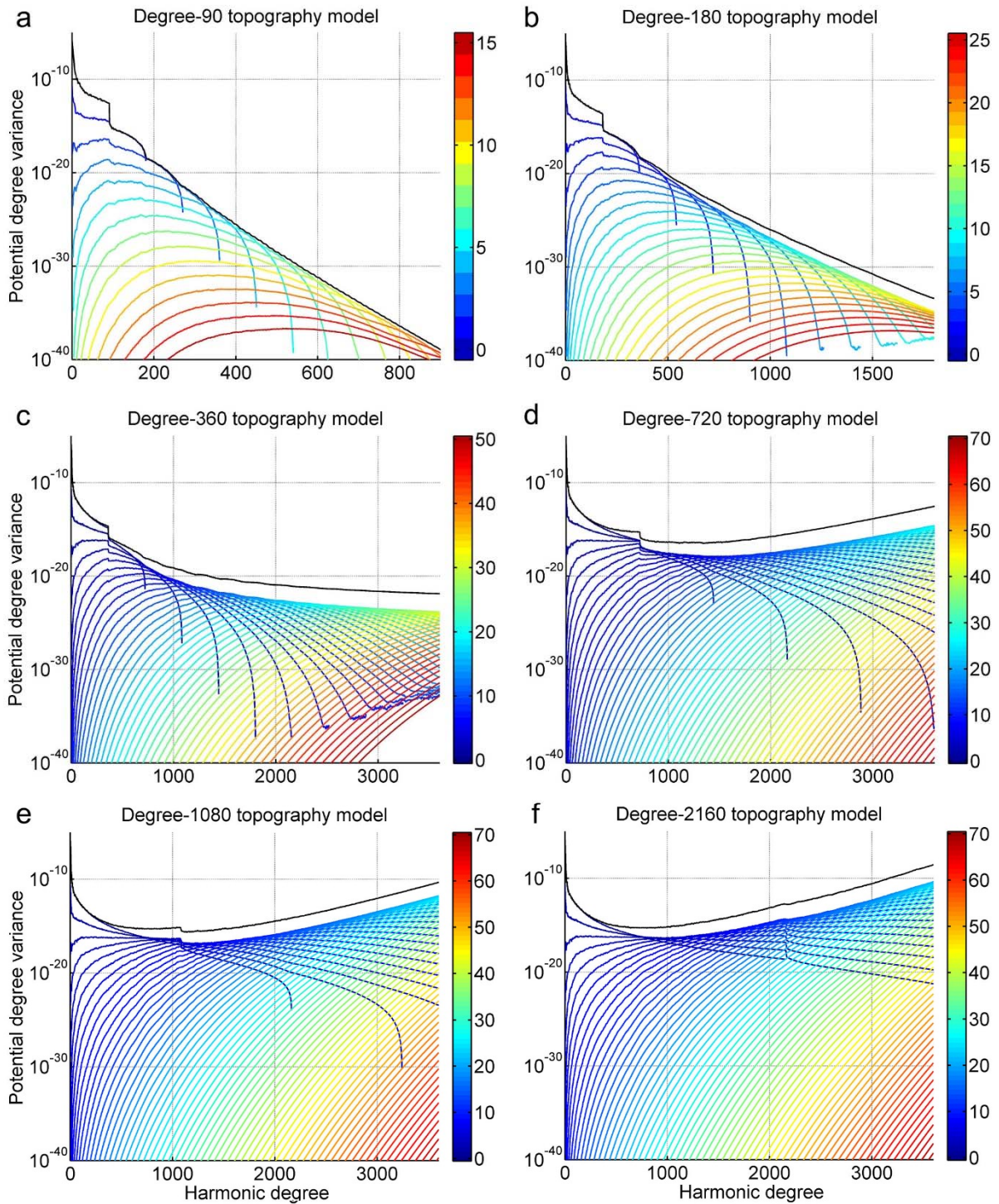
Figure 1. Contributions to the topographic potential made by the integer powers p of the topography (various colors) and (total) topographic potential (black), obtained as sum of the single contributions. Panel a: degree-90 input topography, panel b: degree-180, panel c: degree-360, panel d: degree-720, panel e: degree-1080, panel f: degree-2160 input topography. All panels show dimensionless potential degree variances (cf. Eq. 5). All spectra refer to the reference sphere with R = 1738,000 m.

389 Importantly, Fig. 2 reveals for all six topographic potential models the spectral power beyond the
390 (nominal) resolution N_{max}^T of the input topography, that is, in spectral band $[N_{max}^T + 1 \dots N_{max}^G]$. For
391 the six levels of resolution, these "tails" can be thought of as a set of curves with systematic upward-
392 bending behaviour (Fig. 2). While for lower N_{max}^T the tails quickly drop (showing a rapid decay in
393 short-scale energy), there is a slow decay for $N_{max}^T = 360$, and for larger N_{max}^T, there is an apparent
394 increase in spectral energy observed with increasing n. Additionally, the tails tend to be the more
395 upward-curved, the larger N_{max}^T, and this behaviour might be an indicator for severe divergence of
396 the series in the spatial domain (Section 3.3).
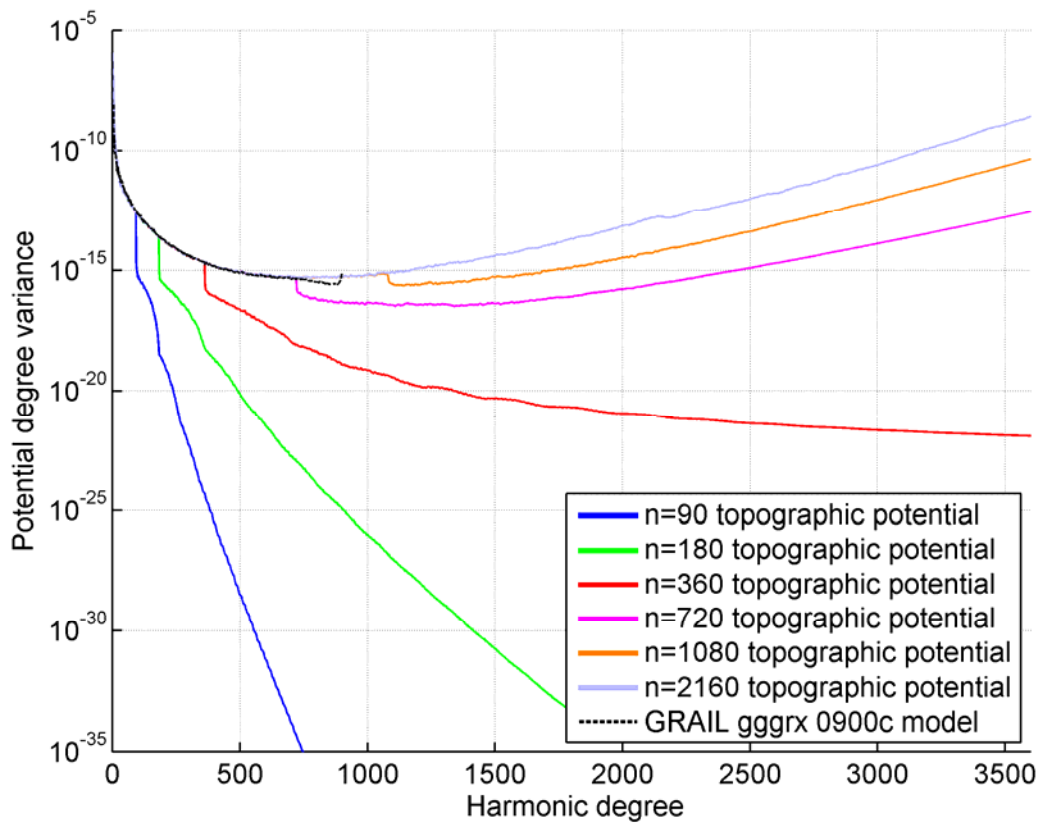
397

398 **Figure 2.** Comparison of potential degree variances of GRAIL GGRX 0900c (model of the observed
399 gravitational potential) with the topographic potential implied by degree-90, 180, 360, 720, 1080 and
400 2160 topography models developed in this work

401 **3.2 Spatial analyses**

402 Gravity values δg from both forward modelling techniques,

403 • the spherical harmonic series (Sect. 2.2.3) and
404 • the discretized numerical integration (Sect. 2.2.4)

405 were compared (a) as a function of the input topography resolution N_{max}^T (Table 1), (b) as a function
406 of the maximum harmonic degree N^G in the gravity syntheses (Eq. 4) and (c) for the four different
407 vertical arrangements of computation points (cases 1-4, Section 2.2.2). The descriptive statistics of
408 the gravity values δg from both techniques, computed at 5 arc-min resolution (2160 x 4320 grid
409 nodes covering the whole of the Moon), are reported in Table 2, and the statistics of differences $\Delta \delta g$
410 between gravity from both techniques are given in Table 3.

411 **Table 2.** Descriptive statistics of the gravity disturbances from NI and SH modelling as a function of the
412 location of evaluation points, the resolution of the topography model N_{max}^T All statistics based on 5
413 arc-min global grids, unit is mGal in all cases.

Case description		Newtonian integration			Spectral modelling with multiples			
Location	Input N_{max}^T	Min	Max	RMS	Output N_{max}^G	Min	Max	RMS
Hsur	90	-1072.3	893.1	332.4	630	-1072.3	893.1	332.4
	180	-1179.7	917.0	339.2	1260	-1179.7	917.0	339.2
	360	-1190.1	1000.5	343.2	3600	-4.6E+04	4.1E+04	390.9
	720	-1173.3	1025.0	345.1	3600	-1.1E+09	1.4E+09	6.6E+06
	1080	-1244.6	1032.4	345.8	3600	-4.3E+11	7.1E+11	1.2E+09
	2160	-1283.5	1024.4	346.3	3600	-2.6E+13	1.1E+13	2.7E+10
Hpos	90	-948.5	893.1	328.3	630	-948.5	893.1	328.3
	180	-1003.6	917.0	332.5	1260	-1003.6	917.0	332.5
	360	-972.2	1000.5	334.4	3600	-972.2	1000.5	334.4
	720	-976.4	1025.0	334.8	3600	-3.0E+04	3.2E+04	384.5
	1080	-976.2	1032.4	334.8	3600	-5.5E+05	5.4E+05	2.4E+03
	2160	-976.3	1024.4	334.8	3600	-5.1E+06	5.2E+6	2.3E+04
H11km	90	-859.4	866.3	317.2	630	-859.4	866.3	317.2
	180	-881.4	878.3	318.2	1260	-881.4	878.3	318.2
	360	-874.1	958.5	318.4	3600	-874.1	958.5	318.4
	720	-874.6	985.6	318.4	3600	-874.6	985.7	318.4
	1080	-874.6	991.0	318.4	3600	-874.6	991.0	318.4
	2160	-874.6	983.8	318.4	3600	-874.6	983.8	318.4
H23km	90	-796.1	770.1	306.9	630	-796.1	770.1	306.9
	180	-806.6	755.0	307.1	1260	-806.6	755.0	307.1
	360	-806.5	766.9	307.1	3600	-806.5	766.9	307.1
	720	-806.5	768.2	307.1	3600	-806.5	768.2	307.1
	1080	-806.5	768.2	307.1	3600	-806.6	768.2	307.1
	2160	-806.5	768.2	307.1	3600	-806.6	768.2	307.1

414

415 Maximum absolute differences, defined as max ($|\Delta\delta g|$) and root-mean-square (RMS) values of $\Delta\delta g$
416 are shown in Fig. 3 for a total of 140 permutations over the three parameters N_{max}^T, N^G and
417 evaluation heights. From top to bottom, the panels are arranged in terms of the increasing
418 evaluation heights (Hsur, Hpos, H11km, H23km, as defined in Sect 2.2.2), and each panel shows the
419 convergence/divergence behaviour for the six topography resolutions N_{max}^T (different colors) as a
420 function of N^G (maximum degree in the gravity syntheses). In most cases, the N^G were chosen such
421 that $N_{max}^T \leq N^G = kN_{max}^T \leq N_{max}^G$, where kN_{max}^T are integer multiples of N_{max}^T. The black solid line in
422 all panels of Fig. 3 marks the 1 mGal threshold that indicates sufficiently accurate representation of
423 gravity through spectral gravity modelling with external harmonics.

424 As the key result of our work, Fig. 3 gives unprecedented detailed insight into the divergence vs.
425 convergence behaviour of the SH series of the Moon's topographic potential, exemplified here via
426 gravity disturbances [cf. Eq. (4)].

427

428 **Table 3.** Descriptive statistics of the gravity differences "SH minus NI", as a function of the location of
429 evaluation points, the resolution of the topography model N_{max}^T and of the resolution of the SH
430 modelling N_{max}^G. All statistics based on 5 arcmin- global grids, unit is mGal in all cases.

Case description		Truncated spectral modelling				Spectral modelling with multiples			
Location	Input N_{max}^T	Output N_{max}^G	Min	Max	RMS	Output N_{max}^G	Min	Max	RMS
Hsur	90	90	-46.535	31.277	2.6425	630	-0.007	0.006	0.0006
	180	180	-79.455	54.772	4.8322	1260	-0.028	0.022	0.0016
	360	360	-130.168	91.242	6.0685	3600	-4.5E+04	4.2E+04	2.0E+02
	720	720	-309.528	254.367	9.4200	3600	-1.1E+09	1.4E+09	7.0E+06
	1080	1080	-3.1E+03	2.6E+03	38.197	3600	-4.3E+11	7.1E+11	1.2E+09
	2160	2160	-2.6E+07	3.3E+07	1.2E+05	3600	-2.6E+13	1.1E+13	2.7E+10
Hpos	90	90	-34.652	31.277	2.3980	630	-0.027	0.037	0.0006
	180	180	-70.373	54.772	4.0004	1260	-0.072	0.188	0.0019
	360	360	-108.713	71.849	4.4135	3600	-0.655	0.724	0.0059
	720	720	-218.709	115.775	4.6511	3600	-3.0E+04	3.3E+04	2.0E+02
	1080	1080	-401.508	343.723	5.8322	3600	-5.4E+05	5.4E+05	2.4E+03
	2160	2160	-1.7E+04	1.8E+04	1.1E+02	3600	-5.1E+06	5.2E+06	2.3E+04
H11km	90	90	-20.984	15.220	1.2658	630	-0.014	0.004	0.0007
	180	180	-23.645	13.976	1.1787	1260	-0.018	0.013	0.0015
	360	360	-20.977	13.179	0.4664	3600	-0.030	0.031	0.0029
	720	720	-9.291	8.975	0.0918	3600	-0.068	0.042	0.0048
	1080	1080	-5.507	5.338	0.0254	3600	-0.145	0.181	0.0063
	2160	2160	-0.750	1.071	0.0075	3600	-0.172	0.260	0.0074
H23km	90	90	-9.159	6.688	0.6024	630	-0.019	0.005	0.0008
	180	180	-4.716	3.241	0.2860	1260	-0.021	0.005	0.0014
	360	360	-0.993	0.685	0.0313	3600	-0.024	0.005	0.0026
	720	720	-0.041	0.043	0.0045	3600	-0.029	0.005	0.0044
	1080	1080	-0.031	0.011	0.0053	3600	-0.031	0.011	0.0053
	2160	2160	-0.034	0.010	0.0063	3600	-0.034	0.011	0.0063

431

432 *Note on the terminology convergence and divergence as used in this study*

433 Here we refer to the term convergence when the residuals between numerical integration and SH
434 series expansions (illustrated in Figure 3) show a steady decrease with increasing maximum spherical
435 harmonic degree. Conversely, we refer to divergence when the residuals start to grow for increasing
436 spherical harmonic degrees. We acknowledge that this interpretation does not relate to
437 convergence or divergence of a series in a purely mathematical sense; it rather indicates the ability of
438 the external spherical harmonic series [Eq. (4)] to accurately represent gravity in the space domain.
439 In this case, the residuals fall below a given threshold (e.g. 1 mGal in Fig. 3). On the other hand,
440 technique limitations are clearly indicated by residuals increasing with harmonic degree or failure to
441 reach a given threshold (Fig. 3), showing the inability of the external harmonic series expansion
442 approach to adequately model near-surface gravity. While the indicators may point towards
443 convergence or divergences, we cannot – in a rigorous mathematical sense - guarantee series
444 convergence or divergence when extending the harmonic series to infinity. This is because we work
445 with truncated series expansions [that is, no evaluation takes place beyond degree N_{max}^G in Eq. (2)
446 and (4)], as is a usual restriction when working with spherical harmonics.
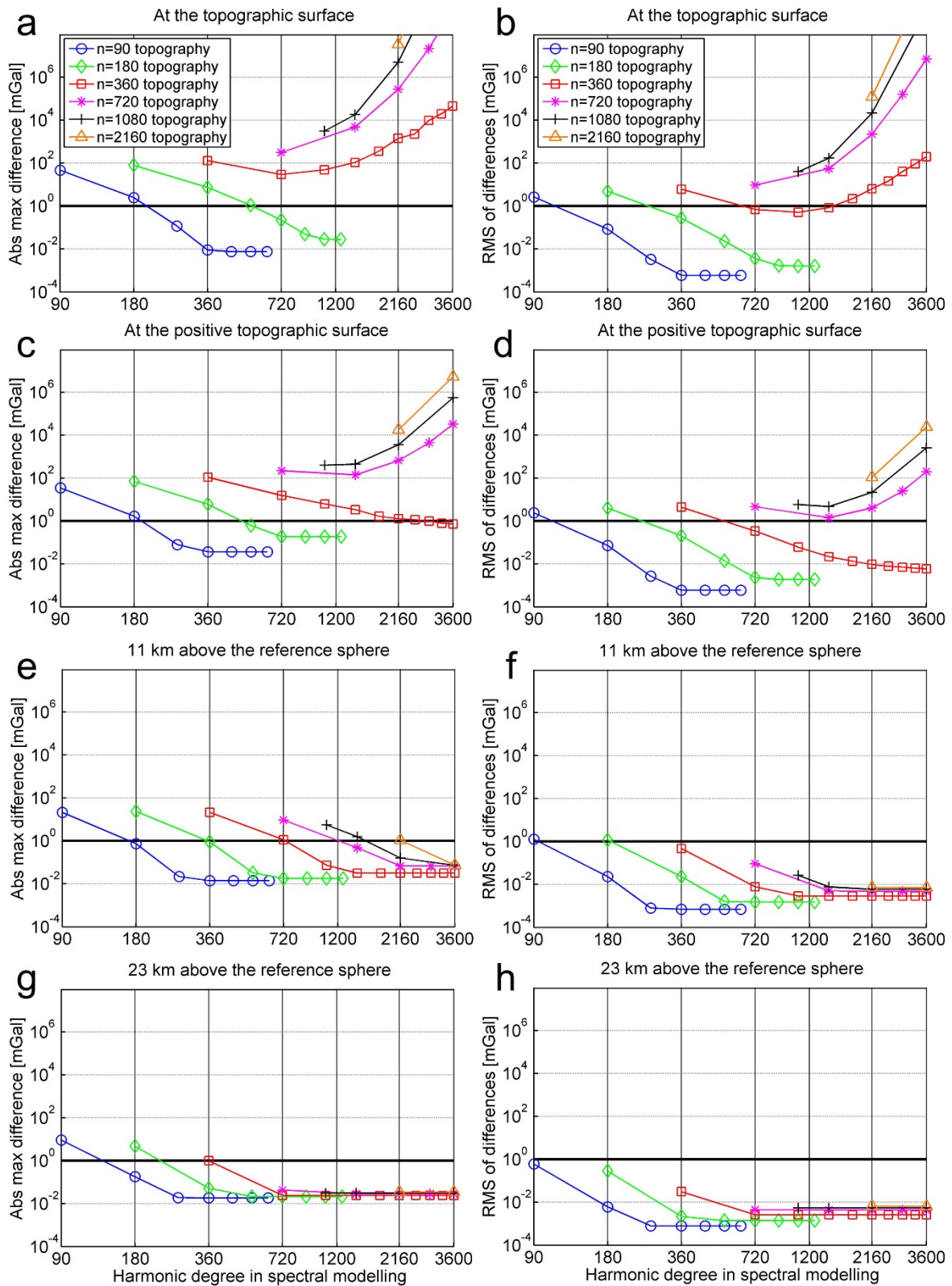
Figure 3. Comparison of gravity from SH and NI as a function of (i) the evaluation height (from top to bottom), of (ii) the resolution of the input topography model (various colors), of (iii) the maximum SH degree considered in the spectral modelling. Left column: absolute maximum of the differences SH minus NI, Right column: RMS (root-mean-square) of the differences. Comparisons based on 5 arc-min global grids; unit on the vertical axis is mGal. The figure shows how convergence and divergence depend on evaluation height and spectral resolution.

3.2.1 Degree-90 and degree-180 topographies

455   For our lowest-resolution topography model ($N_{max}^T = 90$), Fig. 4a shows the gravity values δg from
456   the numerical integration at 2160 x 4320 grid points across the Moon and Fig. 4b the gravity
457   differences $\Delta\delta g$ between the two techniques, whereby the SH series (Eq. 4) was truncated to $N^G =$
458   N_{max}^T, and all computation points reside at the topographic surface with $N_{max}^T = 90$. Fig. 4b shows
459   the spectral inconsistency between gravity from NI and SH when the latter is deliberately truncated
460   to N_{max}^T in the synthesis. It is the short-scale signal produced by the higher-order powers ($p \geq 2$) of
461   the topography $H_{nm}^{(p)}$ at harmonic degrees $N^G > N_{max}^T$ that is reflected by the differences in Fig. 4b. In
462   the present case, these short-scale signals may exceed ~10 mGal amplitudes (cf. Fig. 4b and Table 3,
463   "truncated spectral modelling"). When the spectral modelling is extended to $N^G = 7N_{max}^T = 630$,
464   the short-scale signals are fully modelled and the agreement between both techniques dramatically
465   improves by ~4 orders of magnitude to the level of ~1 µGal (Fig. 4c and Table 3, "spectral modelling
466   with multiples").

467   Fig. 4c reveals excellent agreement which we interpret here as full convergence of the SH series
468   anywhere across the surface of the Moon. The differences in Fig. 4c reflect residual errors in the
469   numerical integration which – if it was necessary – could be further reduced by increasing the
470   oversampling (Sect. 2.2.4). However, these residuals are entirely uncritical for this study, given their
471   very small µGal-level amplitudes. Importantly, the excellent agreement of gravity values computed
472   with two independent techniques from the same topographic mass distribution demonstrates the
473   correct and consistent application of the two techniques, and serves as a baseline ("best-case
474   scenario") for all further comparisons (Table 3).

475   Fig. 4c also reveals that – probably in contrast to common belief – SH models can be accurately
476   evaluated even deep inside the reference sphere (about 50 % of the lunar surface is inside the
477   reference sphere of radius R), provided that the resolution of the field-generating mass model is low
478   enough. For points inside the reference sphere, that is, $r < R$, the factor $(R/r)^n$ – commonly
479   referred to as attenuation or dampening factor in Eq. 4 – reverses it purpose and acts instead as
480   amplification factor. If the gravity signals were not correctly amplified for evaluation points inside R,
481   the agreement between the two methods would not have been as good as shown in Fig 4c. The
482   duality of the amplification vs. attenuation mechanism is not very widely addressed in the literature.

483   Table 3 reports the descriptive statistics for the comparisons of gravity from our $N_{max}^T = 90$
484   and $N_{max}^T = 180$ topography models at for the four different altitudes, and Fig. 3 shows the detailed
485   convergence behaviour of the spherical harmonic solution against the integration solution as a
486   function of N^G (blue line for $N_{max}^T = 90$, green line for $N_{max}^T = 180$). In all cases – irrespective of
487   the point location inside or outside the Brillouin-sphere – the spherical harmonic series fully and
488   accurately converge, which is seen from the $\Delta\delta g$ values being always smaller than 40 µGal for our
489   complete spectral models (Table 3, "Spectral modelling with multiples"). Thus, our experiments
490   suggest that the spherical harmonic gravity models converge anywhere outside the lunar
491   topographic masses when the topography resolution is limited to scales of ~30 km ($N_{max}^T \leq 180$).

492
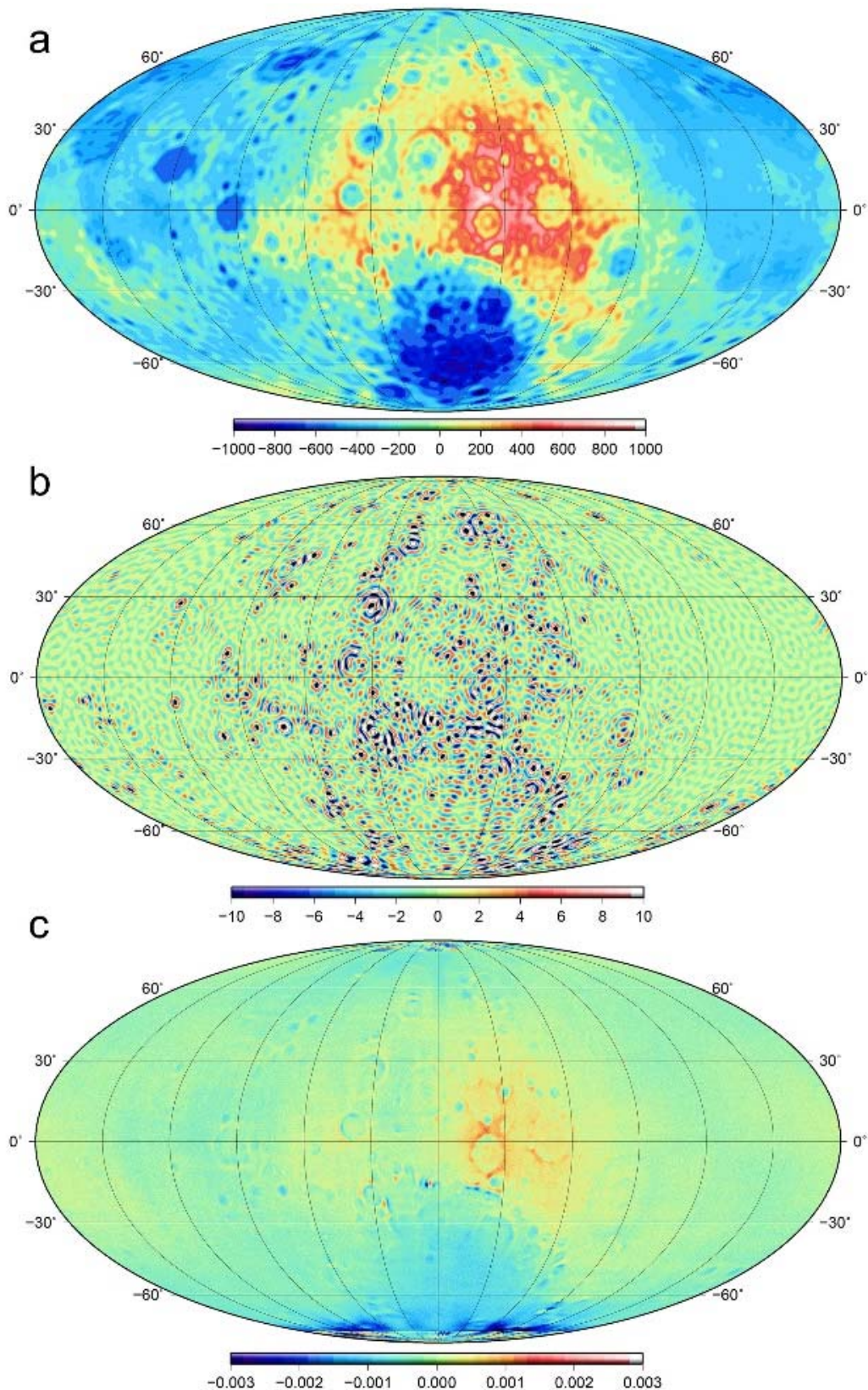
Figure 4. Forward modelling results using the degree-90 topography model. Panel a: Gravity
disturbances from NI, Panel b: Gravity differences "SH modelling to degree 90 minus NI", Panel c:
Gravity differences "SH modelling to degree 630 minus NI"". All gravity values computed at the
topographic surface Hsur. The figure shows the importance of modelling short-scale gravity signals,
beyond the resolution of the input model, to achieve excellent agreement between both techniques
at the microgal level (panel c). Units in mGal.

3.2.2 Degree-360 and degree-720 topographies

Compared to degree-90 and 180 comparisons, the increase to degree-360 resolution marks the "turning point" where the speed of convergence is not only reduced, but divergence starts to become relevant. This is seen from the slowly decreasing discrepancies in Fig. 3b, which do not drop below the ~0.7 mGal level when the $N_{max}^{T} = 360$ model is evaluated to $N^{G} = N_{max}^{G} = 3,600$ at the topography but not inside R (case Hpos, Table 3).

When the evaluation points reside at the topography (case Hsur), maximum absolute difference do not fall below ~70 mGal (see the local minimum in the red curve at $N^{G} = 720$ in Fig. 3a) and rise with increasing N^{G} beyond the level of 10^{4} mGal (Fig. 3). We interpret this behaviour as a clear sign of divergence of the spherical harmonic series attributable to the multiples of the input band-width.
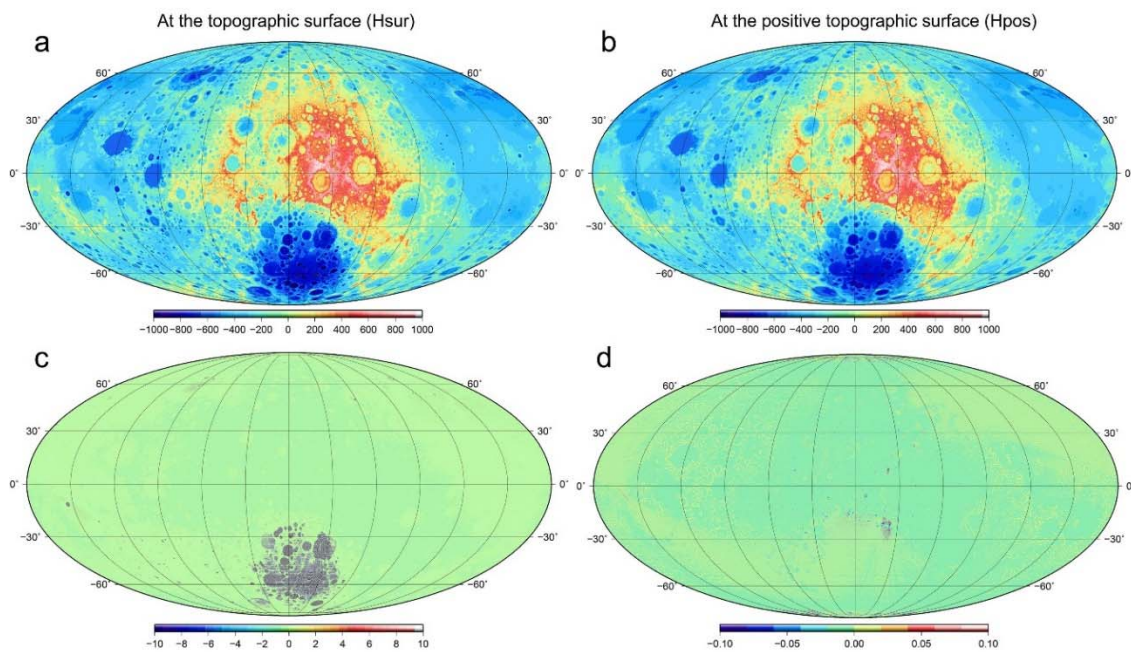
Figure 5. Forward modelling results using the degree-360 topography model. Panel a: Gravity from SH modelling computed at Hsur (positive and negative heights), panel b: same but computed at Hpos (no negative heights), Panel c: Gravity differences "SH minus NI" at Hsur, Panel d: same but at Hpos. Maximum degree in the SH modelling is 2520. The left column shows divergence for computation points in the deep Apollo Basin, while convergence is reached when avoiding negative heights (i.e., lifting the computation points to zero where H<0). Units in mGal.

The spatial distribution of evaluation points subject to divergence is displayed in Fig. 5. Divergence primarily occurs over the deep Apollo basin, where the surface topography points are located deep (up to ~17 km) inside the Brillouin-sphere (Fig. 5a, 5c). Raising these deep evaluation points to R (points become airborne over, e.g., the Apollo basin) eliminates the divergence problem for the $N_{max}^{T} = 360$ topography model (Fig. 5b, 5d). This clearly illustrates the dependence of divergence on the depth of evaluation points inside R_{B}, and, more specifically, on $r < R$, where the $(R/r)^{n}$ factor amplifies the spectral energy.

For our $N_{max}^{T} = 720$ input topography model, the divergence in the spherical harmonic series is seen to exacerbate. For evaluation inside the Brillouin-sphere (cases Hpos and Hsur), maximum absolute differences between gravity from both techniques always exceed 100 mGal (Fig. 3a, 3c). A monotonic increase of the errors with the number of multiples considered in the gravity synthesis is

attributable to divergence in the SH method (Fig. 3a). For $N^G = N_{max}^T$, the gravity differences reflect certainly (i) spectral inconsistency, and possibly (ii) emerging divergence, but discrimination between both effects is difficult.

For degrees of evaluation $N^G > N_{max}^T = 720$, the discrepancies among both methods surge beyond 10^9 mGal (Table 3) and are present over most of the lunar surface (Fig. 6a, 6c). For evaluation points at the topography, but not inside R, divergence effects are smaller but still exceed the 10^4 mGal level (Fig. 6b, 6d). The comparisons between gravity from NI and SH reveal that divergence may originate over moderately undulating topography of the Moon's near-side and "radiate" from what we call here a seed-point over large parts of the planetary surface (Fig. 6d). As a result, gravity values over large surface areas appear to become "contaminated" by divergence, the spatial patterns of which elude their prediction. As the central result of Fig. 6, the SH technique is subject to severe divergence when applied to completely model the $N_{max}^T = 720$ topographic gravity field at the surface of the Moon.
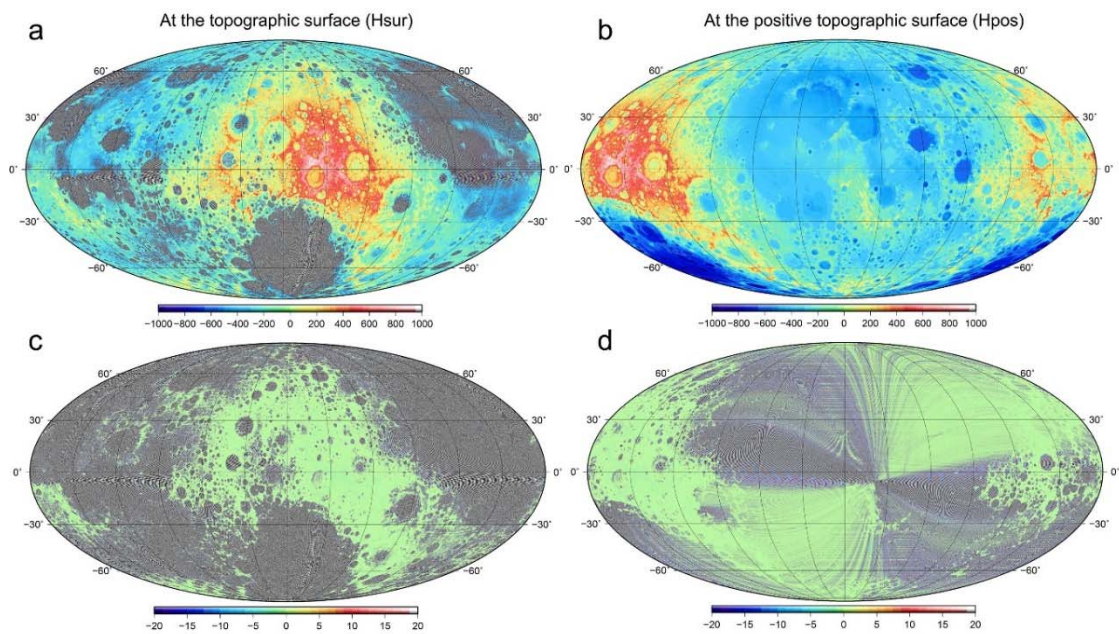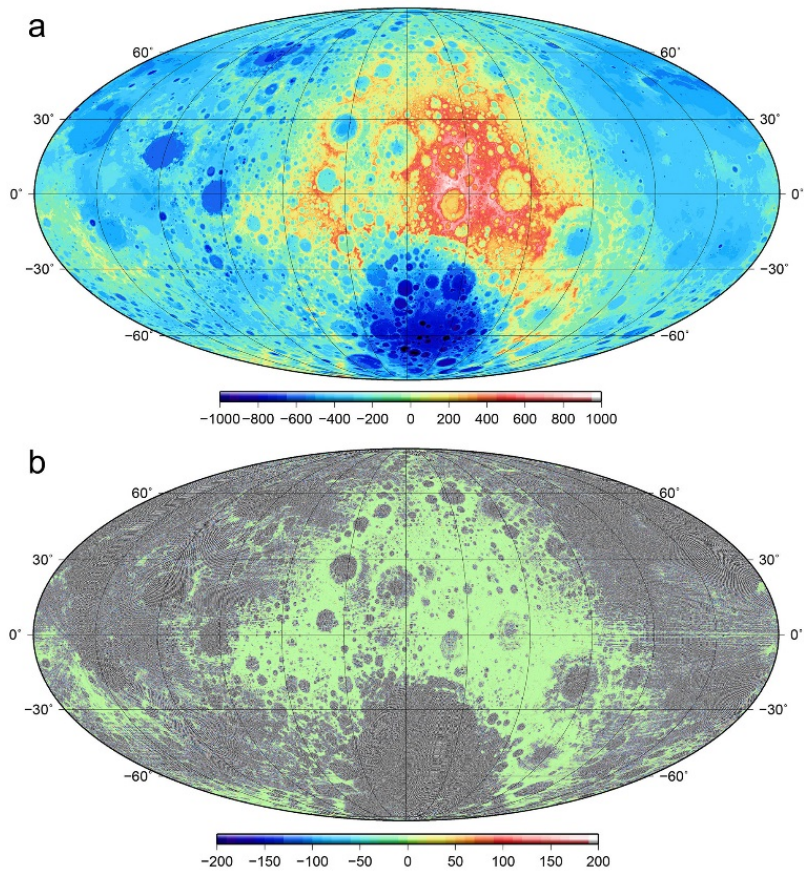

Figure 6. Forward modelling results using the degree-720 topography model. Panel a: Gravity from SH modelling computed at Hsur (positive and negative heights) panel b: same but at Hpos (no negative heights). Panel c: Gravity differences "SH minus NI" at Hsur, Panel d: same but at Hpos. Maximum degree in the SH modelling is 2880. The left column shows severe divergence for most computation points at the topographic surface except at higher elevations.. For Hpos, the right column shows a seed-point near the centre of the near-side with divergence radiating over several 1000 kms. The central meridian in panels c and d has been choosen such that the spatial patterns of divergence become better visible. Units in mGal.

3.2.3 Degree-1080 and degree-2160 topographies

Gravity computed from the $N_{max}^T = 1080$ (2160) topographies is severely affected by divergence when the spectral method is applied at computation points residing at the topography (Hsur). From Table 3, the maximum discrepancies exceed 3,000 mGal ($N^G = N_{max}^T = 1080$) and 3.3×10^7 mGal ($N^G = N_{max}^T = 2160$). Modelling of degrees $N^G > N_{max}^T$ worsens the disagreement with NI (see Table 3 and black/orange curves in Fig. 3a, 3b).

Figure 7. Forward modelling results using the degree-2160 topography model. Panel a: Gravity from NI, panel b: Gravity from SH (evaluated to degree 2160) minus NI at the topographic surface, unit in mGal.
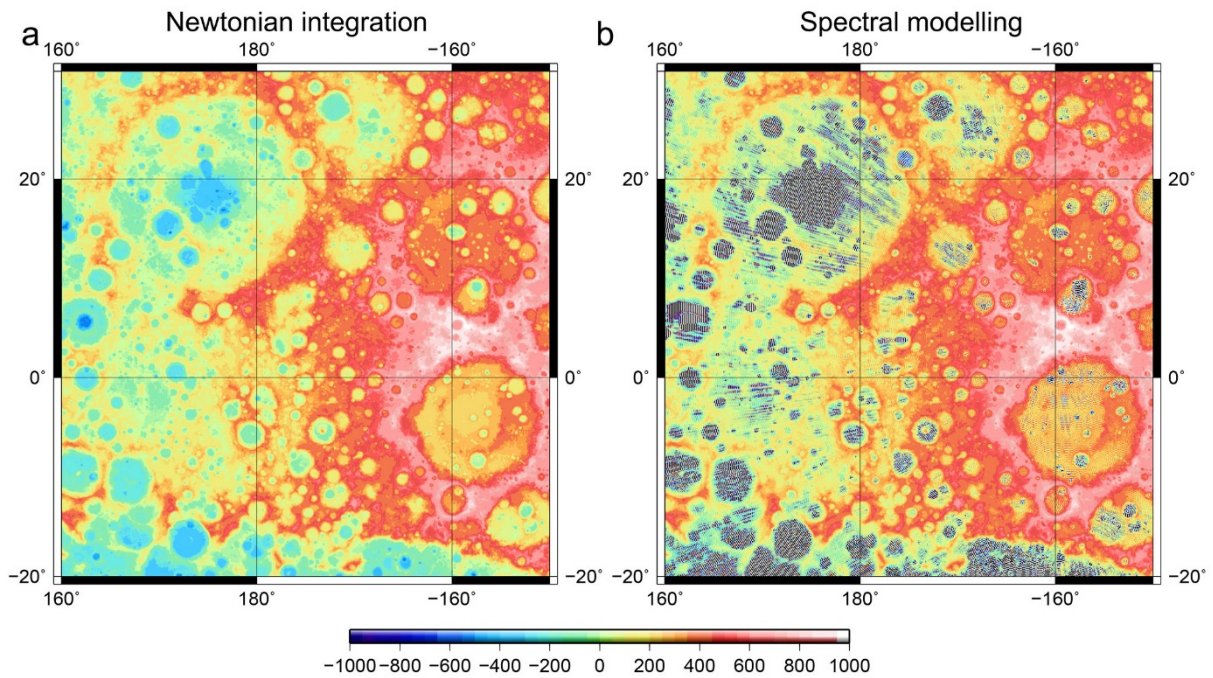
Figure 8. Forward modelling results using the degree-2160 topography model. Panel a: Gravity from NI, panel b: Gravity from SH (evaluated to degree 2160) at the topographic surface, shown over the far-side highlands, unit in mGal.

565   For $N_{max}^T = 2160$ and computation points residing at the topography, Fig. 7a shows gravity from NI
566   and Fig. 7b gravity differences between NI and SH modelling ($N^G = 2160$). From Fig. 7b, the
567   majority of computation points are severely affected by series divergence. Detailed views are given in
568   Fig. 8 over the far-side highlands, one of the – in a relative sense – lesser affected areas. Gravity from
569   the spectral modelling is seen to provide grossly incorrect values inside craters (compare Fig. 8a with
570   Fig. 8b). A characteristic feature of series divergence are extreme short-scale oscillations between
571   large positive and negative values in craters that render the spectral technique inapplicable at such
572   high spectral resolution over rough topography.

573

574   When the computation points are outside the Brillouin-sphere (Figs. 3e – 3h), the agreement
575   between the two gravity modelling techniques is better or much better than the mGal level,
576   corroborating that both techniques deliver correct values that are accurate enough from a practical
577   point of view. For H = 11 km and $N_{max}^T = 1080$, the maximum difference is below 0.2 mGal when
578    $N^G = 3600$, and below 0.3 mGal for $N_{max}^T = 2160$ (cf. Table 3). The maximum differences could
579   possibly be further reduced if the modelling was extended beyond degree 3600. However, this was
580   not attempted in this work (see reasons in Sect. 3.1).

581

582   **3.2.4 Convergence inside vs. outside Brillouin-sphere**

583   From top to bottom, Fig. 3 gives detailed insight into the convergence behaviour of spherical
584   harmonic gravity models as a function of the evaluation height. For evaluation points inside the
585   Brillouin-sphere, our experiments (Fig. 3a and 3c) demonstrate that the spherical harmonic series
586   may converge or may diverge. Convergence is guaranteed for low spatial resolutions only (in our
587   study up to $N_{max}^T = 180$), while with higher-resolution mass/gravity models, convergent series turn
588   into divergent ones, and, as a result, invalid gravity values are obtained. The divergence effect is seen
589   to be the stronger, the deeper the computation points reside inside the Brillouin-sphere, and the
590   finer the resolution of the gravity modelling (see Fig. 3a and 3c).

591   However, for evaluation points at R_B (Brillouin-sphere, 11 km above R) or at GRAIL-altitude R_G (23
592   km above R) all SH series expansions are consistently seen to converge toward the NI solutions (Fig.
593   3e and 3g). This is evident from the very good mutual agreement among the gravity values. The
594   maximum absolute differences are always smaller than ~0.3 mGal (Table 3), and convergence for
595   gravity from the $N_{max}^T = 360$ topography is reached at degree $N^G = 1440$ at R_B and $N^G = 720$ at
596   R_G. This is seen from the fairly horizontal graphs beyond the reported N^G values.

597   For gravity from the $N_{max}^T = 720$ model, there is no need to evaluate gravity at R_B beyond $N^G =$
598   2,160, while this value is lower at GRAIL altitude R_G ($N^G = 1,440$) because the points are even
599   farther away from the mass distribution, so short-scale signals are more attenuated as a
600   consequence of Newton's law of gravitation.

601   Thus, outside the Brillouin sphere, the series expansions converge against the independent NI
602   solution in any case (Fig. 3c and 3d), irrespective of the gravity model resolution or location of points
603   outside that sphere. As such the outcome of our experiments fully support the theory of external
604   spherical harmonics [*Moritz*, 1980; *Takahashi and Scheeres*, 2014; *Hu and Jekeli*, 2015].

605   **3.3 The relation between degree variances and divergence inside the Brillouin-sphere – a new**
606   **hypothesis**

607   Generally, convergence of exterior spherical harmonics inside the Brillouin-sphere is rightly
608   considered a highly "unstable phenomenon" [see *Hu and Jekeli*, 2015], and divergence behaviour can

609 be considered difficult to predict. However, a cross comparison between the degree variances of the
610 topographic potential models (Fig. 2) and the behaviour of the spherical harmonic series expansions
611 inside the Brillouin sphere (Fig. 3a, 3b) suggests that the power spectra possibly contain valuable
612 clues as to whether the series might be subject to divergence in free-space bounded by the surface
613 of the mass-distribution and the Brillouin-sphere. Relating Fig. 2 with Fig. 3a (3c) shows for
614 topographic potential models of the Moon

- convergence anywhere at or outside the topographic surface if the spectral energy of the potential quickly decays with N^G (blue and green line, $N^T_{max} = 90$ and 180),
- the possibility of divergence at points deep within the Brillouin-sphere if the spectral energy shows very slow decay with harmonic degree N^G (red line, resolution $N^T_{max} = 360$), and
- certainly occurring divergence somewhere inside the Brillouin-sphere if the spectral energy associated with the input-bandwidth or multiples thereof rises for high harmonic degrees (e.g., purple line ($N^T_{max} = 720$), beyond $N^G = 1200$; light blue line ($N^T_{max} = 2160$), beyond $N^G = 800$).

623 Based on these observations, we formulate a new hypothesis to predict divergence of the spherical
624 harmonic series, solely from the spectral-domain behaviour:

625 A *minimum in the degree variances of an external potential model foreshadows divergence of the*
626 *spherical harmonic series expansions at points inside the Brillouin-sphere.*

627 This hypothesis is supported by all of our numerical experiments, so is valid for the gravity fields
628 implied by our topographic mass models and the six levels of resolution investigated. However, for
629 planetary gravity fields of bodies other than the Moon, further numerical tests are needed to
630 in/validate our hypothesis.

631 One could be tempted to argue that the harmonic degrees N^G with ascending spectral power
632 beyond the local minimum (Fig. 2) should not be included in the gravity synthesis. However, for
633 computation points outside the Brillouin-sphere, our numerical study has demonstrated the validity
634 and importance of – at least some of – these harmonics for the computation of correct gravity
635 values. For instance, SH gravity from the N^T_{max}-1080 topography differs from NI by up to 5.6 mGal
636 when evaluated to $N^G = 1,080$ at the Brillouin-sphere, while the maximum discrepancies are less
637 than 0.2 mGal when $N^G = 3,600$ (Table 3).

4 Discussion and conclusions

639 The present study offers new detailed insights into the matter of divergence vs. convergence of
640 spherical harmonic series expansions of the gravitational potential, by using forward-modelled
641 gravity of Earth's Moon as example. A set of topographic mass models of varying resolution (from 61
642 to 2.5 km detail) was constructed and the implied gravitational fields were computed at four sets of
643 heights with spherical harmonic series and numerical integration, whereby the latter technique is not
644 subject to the divergence problem. The numerical experiments considered the current state-of-the-
645 art for technique comparisons (Sect. 2), including very short-scale signal modelling in spherical
646 harmonics and highly-oversampled numerical integration to reach mutual consistency at the micro-
647 Gal level. For all models and levels of resolution, spherical harmonic series of the gravitational
648 potential were shown to be convergent outside the Brillouin-sphere, as expected from the theory.

649 Our numerical study has shown the spherical harmonic series of the gravitational potential to fully
650 converge in free-space inside the Brillouin-sphere to ~30 km resolution (degree-180) of the field-
651 generating topographic mass model. Thus, gravity functionals from exterior gravitational potential

652   models with similar resolution and characteristics can be adequately modelled with spherical
653   harmonic series down to the lunar surface.

654   For mass models of degree-360 or higher resolution, divergence was shown to become relevant. For
655   degree-360 models, the spherical harmonic diverge for evaluation points that are deepest inside the
656   Brillouin-sphere when the implied gravity field is computed with full detail, i.e., also short-scale
657   gravity signals beyond the degree-360 resolution are considered. For degree-720 resolution mass
658   models, divergence prevents complete gravity modelling with spherical harmonics for the majority of
659   surface topography points, and this exacerbates for degree-1080 and degree-2160 topography
660   models used in the forward-modelling. In case of the degree-2160 topography model divergence is
661   evidently present when gravity is synthesized to degree-2160 at the lunar topography (Fig. 7 and 8),
662   preventing the use of the spherical harmonic technique – as described in Sect. 2 – from applications,
663   such as prediction of gravity values at the lunar topography resolved to ~2.5 km. This finding is
664   important, e.g., if degree-2160 spherical harmonic gravity models (with the high degrees predicted
665   from topography) were to be used to compute gravity along spacecraft landing trajectories near the
666   lunar surface.

667   For the degree-720 and degree-1080 resolution levels – which are commensurate to the resolution of
668   GRAIL gravity field models – our study suggests that series convergence at the lunar topography
669   should be considered doubtful. While our numerical experiments unambiguously reveal divergence
670   occurring when the multiples of the input-band width are evaluated, divergence cannot be excluded
671   when the resolution of the implied gravity field model is truncated to those of the topography model.

672   Drawing an analogy between spectral gravity forward modelling for Earth and Moon using degree-
673   2160 topography models, the dependency of series divergence on the ruggedness of topography
674   becomes clear. For Earth, spherical harmonic series were shown to sufficiently converge at the
675   surface of the topography (heights above zero) for degree-2160 topographic gravity models [*Hirt et
676   al.,* 2016], while for the Moon severe series divergence is evident for the gravity models of the same
677   resolution class. This different behaviour of the series for Earth and Moon needs further investigation
678   in a follow-up study.

679   In order to exclude numerical accuracy problems as cause for the high-frequency behaviour of the
680   spectra shown in Fig. 1 and the numerical results (Fig. 3 – 8, Tab. 2 and 3), we have performed
681   numerous tests for both the spectral domain approach (Eqs. 2 to 4) and the numerical integration
682   technique. These included closed-loop tests for the former and comparison to analytical solutions for
683   the gravitational effect of a spherical shell for the latter technique. Our tests conclusively showed
684   that numerical problems cannot explain the results of this study. Furthermore, our results are in line
685   with other studies on the divergence problem [e.g., Hu and Jekeli, 2015; Reimond and Baur, 2016]
686   that attribute series divergence as cause for invalid values produced by the spectral technique inside
687   the Brillouin-sphere.

688   As a central result of this study, a new hypothesis was formulated that relates the spectral-domain
689   behaviour of the gravity models to divergence in the spatial domain. Following our hypothesis, if the
690   potential degree variances show a minimum, then the spherical harmonic series expansions diverge
691   somewhere inside the Brillouin-sphere. The hypothesis is fully supported by our numerical study for
692   the Moon, but its generalisation requires further modelling experiments for other planetary bodies,
693   e.g., Mars and Earth.

694   In summary, by comparing the external potential series expansions (Sect. 2.2.3) with numerical
695   integration (Sect. 2.2.4) for a set of topographic mass models with increasing level of detail (Sect.
696   2.1), our numerical study (Sect. 3) shows the cases in which

697   •   the use of external potential series is good enough to accurately model the topographic
698   potential, and, conversely,
699   •   the external potential series diverge, which is exactly when the internal potential cannot be
700   neglected anymore in case the spectral modelling techniques are applied inside the Brillouin-
701   sphere.

702 The divergence is most likely the result of modelling the gravitational effect of masses above the
703 computation point with external spherical harmonics, showing the importance of the internal
704 potential in those cases.
705
706 Therefore, this paper has shown the limitations of the popular and widely used external potential
707 expansions when used to model the near-surface gravity field implied by planetary topography
708 beyond a certain level of resolution. To avoid divergence issues in such cases, either Newtonian
709 integration (as done in our study) or the 2-potential-method (Bruce Bills, pers. comm. 2017) can be
710 used as alternatives. However, the combination of interior with exterior potential expansions, as
711 done in the 2-potential-method, is radius-dependent (as noted in *Takahashi et al.* [2013], p 364),
712 potentially requiring several 100s of coefficient sets to describe the gravity field implied by planetary
713 topography. As such, both the 2-potential-method and Newtonian integration are computationally
714 rather intensive and do not deliver solid spherical harmonic coefficients without further
715 transformations (e.g., downward-continuation of surface gravity). While our study showed the
716 limitations of external harmonics near rough topography, it also indicates the level of resolution (in
717 case of the Moon: degree ~180 or somewhat higher), when external potential modelling only is free
718 of divergence, as measured by small differences to the Newtonian integration, such that the internal
719 potential can be safely neglected. As future work, the 2-potential-method should be further
720 explored and systematically compared with Newtonian integration.

728 **Data statement**
729
730 The models developed in this work will be made available via http://ddfe.curtin.edu.au/models/ and
731 also distributed via archives http://icgem.gfz-potsdam.de/ICGEM/ and http://geo.pds.nasa.gov/.

Literature

Balmino, G., N. Vales, S. Bonvalot and A. Briais (2012), Spherical harmonic modelling to ultra-high degree of Bouguer and isostatic anomalies, *J. Geod.,* 86(7), 499-520, doi: 10.1007/s00190-011-0533-4.

Blakeley, R.J. (1996), Potential Theory in Gravity and Magnetic Applications. Cambridge: Cambridge University Press.

Bucha, B,. and Janák, J. (2013) A MATLAB-based graphical user interface program for computing functionals of the geopotential up to ultra-high degrees and orders. *Comp. and Geosci.,* 56, 186–196, doi: 10.1016/j.cageo.2013.03.012.

Bucha, B., and Janák, J. (2014) A MATLAB-based graphical user interface program for computing functionals of the geopotential up to ultra-high degrees and orders: Efficient computation at irregular surfaces, *Comp. and Geosci.*, 66, 219-227, doi: 10.1016/j.cageo.2014.02.005.

Chao, B.F., and D.P. Rubincam (1989), The gravitational field of Phobos. Geophysical Research Letters 16(8), 859-862.

Featherstone, W. E., C. Hirt, and M. Kuhn (2013) Band-limited Bouguer gravity identifies new basins on the Moon, *Journal Geophysical Research* (*JGR*) *Planets* 118:1-17, doi:10.1002/jgre.20101.

Forsberg R. (1984), A study of terrain reductions, density anomalies and geophysical inversion methods in gravity field modelling. Report 355, Dep. of Geodetic Sci. Surveying, Ohio State Univ., Columbus.

Fukushima T. (2012), Numerical computation of spherical harmonics of arbitrary degree and order by extending exponent of floating point numbers. *J. Geod.,* 86(4), 271–285, doi: 10.1007/s00190-011-0519-2.

Goossens, S., K. Matsumoto, Q. Liu et al. (2011), Lunar gravity field determination using SELENE same-beam differential VLBI tracking data. Journal of Geodesy 85(4), 205-228, doi:10.1007/s00190-010-0430-2.

Heck, B., and K. Seitz (2007), A comparison of the tesseroid, prism and point-mass approaches for mass reductions in gravity field modelling. *J. Geod*., 81(2) 121-136. doi:10.1007/s00190-006-0094-0

Hirt, C. (2012), Efficient and accurate high-degree spherical harmonic synthesis of gravity field functionals at the Earth's surface using the gradient approach, *J. Geod.,* 86(9), 729-744, doi:10.1007/s00190-012-0550-y.

Hirt C, Featherstone WE (2012) A 1.5 km-resolution gravity field model of the Moon. Earth Planet Science Letters, 329-330, 22-30, doi:10.1016/j.epsl.2012.02.012.

Hirt, C., and M. Kuhn (2012), Evaluation of high-degree series expansions of the topographic potential to higher-order powers, *J. Geophys. Res.,* 117, B12407, doi:10.1029/2012JB009492.

Hirt, C., and M. Kuhn (2014), Band-limited topographic mass distribution generates full-spectrum gravity field: Gravity forward modeling in the spectral and spatial domains revisited *J. Geophys. Res.,* 119(4), 3646-3661, doi: 10.1002/2013JB010900.

Hirt, C**.**, E. Reußner, M. Rexer, and M. Kuhn (2016), Topographic gravity modelling for global Bouguer maps to degree 2,160: Validation of spectral and spatial domain forward modelling techniques at the 10 microgal level, *J. Geophys. Res.* 121(9), 6846–6862, doi: 10.1002/2016JB013249.

Hu, X. (2012), A comparison of ellipsoidal and spherical harmonics for gravitational field modeling of non-spherical bodies. Report No 499, Geodetic Science, The Ohio State University, Columbus, Ohio.

Hu, X. and C. Jekeli (2015), A numerical comparison of spherical, spheroidal and ellipsoidal harmonic gravitational field models for small non-spherical bodies: examples for the Martian moons. J. Geodesy 89, 159–177.

Jackson, J.D. (1962), Classical Electrodynamics. Wiley, New York, London, Sydney.

Jekeli, C. (1983), A numerical study of the divergence of spherical harmonic series of the gravity and height anomalies at the Earth's surface. Bull. Géod. 57, 10–28.

Krarup, T. (1969), A contribution to the mathematical foundation of physical geodesy. In: (ed. Borre, K. 2006) Mathematical Foundation of Geodesy: Selected Papers of Torben Krarup. Springer, Berlin (1969).

Konopliv, A. S., R.S. Park, D.-N. Yuan et al. (2014), High-resolution lunar gravity fields from the GRAIL Primary and Extended Missions, Geophys. Res. Lett., 41, 1452–1458, doi:10.1002/2013GL059066.

Kuhn M., W.E. Featherstone, and J.F. Kirby (2009) Complete spherical Bouguer gravity anomalies over Australia. Australian J. Earth Sci 56(2):213-223, doi:10.1080/08120090802547041.

Kuhn, M., and C. Hirt (2016), Topographic gravitational potential up to second-order derivatives: an examination of approximation errors caused by rock-equivalent topography (RET), *Journal of Geodesy* 90(9), 883-902, doi:10.1007/s00190-016-0917-6.

Lemoine, F.G., S. Goossens, T.J. Sabaka, J.B.Nicholas, E. Mazarico, D.D. Rowlands, B.D. Loomis, D.S. Chinn, G.A. Neumann, D.E. Smith and M.T. Zuber (2014), GRGM900C: A degree-900 lunar gravity model from GRAIL primary and extended mission data. Geophysical Research Letters 41(10): 3382–3389.

Lowes F.J., and D.E. Winch (2012), Orthogonality of harmonic potentials and fields in spheroidal and ellipsoidal coordinates: application to geomagnetism and geodesy. Geophys. J. Int. (2012) 191, 491–507 doi: 10.1111/j.1365-246X.2012.05590.x

789 Moritz., H. (1961), Über die Konvergenz der Kugelfunktionentwicklung für das Aussenraum-Potential an der
790   Erdoberfläche. Österr. Z.f. Vermessungswesen 49.
791 Moritz, H. (1978), On the convergence of the spherical harmonic expansion for the Geopotential at the Earth's
792   surface. Bolletino di Geodesia e Scienze Affini, No 2-3.
793 Moritz, H. (1980), Advanced physical geodesy, Wichmann Verlag.
794 Pavlis, N.K. (2014), Spherical Harmonic Analysis Applied to Potential Fields. In: Encyclopedia of Solid Earth
795   Geophysics, Part of the series Encyclopedia of Earth Sciences Series, pp 1382-1392, Springer, Berlin,
796   Heidelberg, doi 10.1007/978-90-481-8702-7_138.
797 Rapp, R.H. (1989), The decay of the spectrum of the gravitational potential and the topography for the Earth
798   Geophys. J. Int. (1989) 99, 449-455.
799 Rexer, M, C. Hirt, S.J. Claessens, and R. Tenzer (2016), Layer-based modelling of the Earth's gravitational potential
800   up to 10km-scale in spherical harmonics in spherical and ellipsoidal approximation, *Surveys in Geophysics*
801   37(6), 1035-1074, doi:10.1007/s10712-016-9382-2.
802 Rexer, M., and C. Hirt (2015), Ultra-high degree surface spherical harmonic analysis using the Gauss-Legendre
803   and the Driscoll/Healy quadrature theorem and application to planetary topography models of Earth,
804   Moon and Mars. *Surveys in Geophysics* 36(6), 803-830, doi: 10.1007/s10712-015-9345-z.
805 Reimond, S., and O. Baur (2016), Spheroidal and ellipsoidal harmonic expansions of the gravitational potential of
806   small Solar System bodies. Case study: Comet 67P/Churyumov-Gerasimenko, J. Geophys. Res. Planets,
807   121, 497–515, doi:10.1002/2015JE004965.
808 Rummel, R., R. H. Rapp, H. Sünkel, and C. C. Tscherning. (1988), Comparisons of global topographic/isostatic
809   models to the Earth's observed gravity field. Report No 388, Dep. Geodetic Sci. Surv., Ohio State Univ.,
810   Columbus, Ohio.
811 Shen, W. (2009), Convergence of spherical harmonic series expansion of the Earth's gravitational potential, Geo-
812   spatial Information Science, 12:1, 1-6, doi: 10.1007/s11806-009-0180-6.
813 Smith, D.E., Zuber, M.T., Neumann, G.A. et al. (2010), Initial observations from the Lunar Orbiter Laser Altimeter
814   (LOLA). Geophys. Res. Lett. 37, L18204. doi:10.1029/2010GL043751.
815 Sjöberg, L. (1980), On the Convergence Problem for the Spherical Harmonic Expansion of the Geopotential at the
816   Surface of the Earth, Bollettino di Geodesia e Scienze Affini, 39(3), 261—270.
817 Sneeuw, N. (1994), Global spherical harmonic analysis by least-squares and numerical quadrature methods in
818   historical perspective, Geophys. J. Int. 118, 707-716, DOI: 10.1111/j.1365-246X.1994.tb03995.x.
819 Takahashi, Y., D.J. Scheeres, and R.A. Werner (2013), Surface gravity fields for asteroids and comets. J. Guid.
820   Control Dyn. 36(2), 362–374.
821 Takahashi Y. and D. J. Scheeres (2014), Small body surface gravity fields via spherical harmonic expansions. Celest
822   Mech Dyn Astr (2014) 119, 169–206, doi:10.1007/s10569-014-9552-9.
823 Tenzer, R. (2005), Spectral domain of Newton's integral, Boll Geod. Sci. Affini, 2, 61-73.
824 Tsoulis, D. (2012), Analytical computation of the full gravity tensor of a homogeneous arbitrarily shaped
825   polyhedral source using line integrals, Geophysics 77(2), F1-F11, DOI: 10.1190/geo2010-0334.1.
826 Wang, Y.M. (1997), On the error of analytical downward continuation of the earth's external gravity potential on
827   and inside the earth's surface, J. Geodyn., 71(2), 70–82.
828 Werner, R.A. and D.J. Scheeres (1997), Exterior gravitation of a polyhedron derived and compared with harmonic
829   and mascon gravitation representations of asteroid 4769 Castalia. Celestial Mechanics and Dynamical
830   Astronomy 65:313-344.
831 Wieczorek, M.A., and R.J. Phillips (1998), Potential anomalies on the sphere: Applications to the thickness of the
832   lunar crust, *J. Geophys. Res.,* 103(E1), 1715-1724, doi:10.1029/97JE03136.
833 Wieczorek, M.A., et al. (2013), The Crust of the Moon as Seen by GRAIL, Science, 339(6120), pp. 671-675,
834   doi:10.1126/science.1231530.
835 Wieczorek, M.A. (2015), Gravity and Topography of the Terrestrial Planets. In: Schubert G (ed) *Treatise on
836   Geophysics*, 2nd edition, Oxford, 153-193, doi:10.1016/B978-0-444-53802-4.00169-X.
837 Zuber, M.T., D.E. Smith et al. (2013), Gravity Field of the Moon from the Gravity Recovery and Interior Laboratory
838   (GRAIL) Mission, Science 339(6120), 668-671. doi:10.1126/science.1231507.